Computational Particle Mechanics (2019) 6:591–609
https://doi.org/10.1007/s40571-019-00236-1

# Comparison of two numerical approaches (DEM and MPM) applied to unsteady flow

**Fabio Gracia**[1,2] · **Pascal Villard**[2] · **Vincent Richefeu**[2]

Received: 28 January 2019 / Revised: 22 March 2019 / Accepted: 25 March 2019 / Published online: 3 April 2019
© OWZ 2019

**Abstract**
In order to provide a comprehensive comparison between two current numerical methods employed in the modelling of rock avalanches, the discrete element method (DEM) and the material point method (MPM) were used to simulate the mass propagation along a 45° plane transitioning to a horizontal plane. For the DEM simulations, an in-house 3D code whose particles can be modelled as tetrahedral elements was used. Additionally, the flow was canalised using frictionless walls. For the MPM simulations, a 2D code was also developed and employed to run plane strain simulations. Comparisons were made in terms of runout distance, spreading and energy dissipated. Influence of parameters such as initial sample geometry, basal friction coefficient and shape of blocks composing the sample was studied. We found that there are proper correlations between the two methods when the basal friction coefficient has a low value, or when the rolling of the blocks is hindered by using elongated shapes for the blocks. These correlations become less satisfactory as the basal friction coefficient is increased, due to the oversimplified constitutive law employed in MPM.

**Keywords** Discrete element method · Material point method · Continuum · Transitional flow

## 1 Introduction

In this paper, numerical studies involving DEM and MPM were carried out in order to test the ability and the relevance of two kinds of numerical methods (discrete [8,21,27–29,31] and continuous [14,17,22] methods) to reproduce the kinematics of granular avalanches (propagation distances and amounts of dissipated energies). In the field of rock mechanics, the continuum approaches [3,11,20,24,32] are generally considered when large volumes (i.e., large number of blocks) are involved. For this study, the MPM was chosen over other continuum-based methods because of its hybrid Lagrangian and Eulerian descriptions, which gives it the ability to manage naturally large deformations. This makes it an ideal method for the modelling of granular avalanches involving large masses. However, the continuity assumption may also limit the domain of validity of continuum approaches, specifically when dealing with rock flows involving a relatively small amount of blocks. Additionally, the computational times required by the MPM simulations are significantly low, but the dissipation means, and more generally the rheologies, have to be given explicitly by macroscopic constitutive laws with, unavoidably, the continuity of the medium in mind.

On the other hand, the DEM requires an accurate definition of block shapes, suitable roughness of the terrain, together with quite long computational durations. As a consequence, DEM turns out to be more appropriate for "small- or medium-sized volumes" (i.e., few hundred blocks) or more generally when the blocks are prone to separating from each other [4].

Moreover, the complex rheologies inherent in granular materials are naturally well captured by the DEM—provided that a minimum set of features are taken into account. In our case, these features are the block shapes and adequate dissipative contact models. The price to pay is, however, long computational times.

The aim of this paper is to compare the two types of methods on the basis of numerical simulations that consist on the release, first, of randomly packed bricks on an inclined biplane, and second, of a continuum mass governed by an

**Electronic supplementary material** The online version of this article (https://doi.org/10.1007/s40571-019-00236-1) contains supplementary material, which is available to authorized users.

✉ Vincent Richefeu
Vincent.Richefeu@3sr-grenoble.fr

[1] IMSRN, 38330 Montbonnot, France

[2] Univ. Grenoble Alpes, CNRS, Grenoble INP, 3SR, 38000 Grenoble, France

elasto-plastic law for the MPM. These numerical simulations were inspired by small-scale laboratory experimental tests [15,16] that were themselves aimed to validate the discrete element model.

A total of 27 configurations were set up using both numerical methods in order to appreciate the relevance of each approach and to study the influence of some specific parameters related to the released mass, geometry, the basal friction or the shape of the blocks composing the sample (the latter affecting DEM only).

## 2 Discrete element model

One commonly used method that uses a discontinuous approach is the discrete element method (DEM). It was initially developed by Cundall [9] and Cundall and Strack [10] for the modelling of problems in rock mechanics. In this method, each particle is modelled as a single element, where the motions, translation and rotation, are independent. The particle interaction, with other elements or boundary conditions, is governed by contact laws (normal and tangential). These interactions between particles can be modelled in complex ways to allow elastic, plastic, purely frictional or viscous [8] (among others) contact between the particles. Additionally, the shape and size of the particles can vary depending on the type of problem to be modelled. The DEM is thus a very relevant method for applications where the apparent rheology originates at the grain scale. During a time step, motion equations are solved for each particle, taking into account the forces due to contact or collision with other particles, to gravity and to external forces. This is fairly classic, but the key features of the developed code include (1) the shape of the blocks modelled by spheropolyhedra and (2) the scope for dissipation introduced in the collision laws by accounting for the normal, tangential and rotational directions.

From a mathematical point of view, spheropolyhedra are the sum of polyhedra and spheres, but they are processed numerically as rigid aggregates (clumps) of thick polygons for faces, tube for edges and spheres for vertices; this is deeply covered in [23]. Unlike the spheres, the number of contact points between two spheropolyhedra can easily reach high scores—especially for concave shapes. This contributes to a significantly richer overall response of block assemblies when they flow. The contact-or-collision laws can thus be quite simple provided that representative mechanisms of dissipation are accounted for. As usual in DEM, force laws are defined from local variables that are, in the present case, the increment of overlap $\Delta h_n$ and of relative displacement $\Delta h_t$ in the tangential direction, both quantified over a time step [18].

The type of force law used in our application follows the procedure proposed by Banton et al. [1], which is promptly outlined below. In the normal direction, when the overlap is

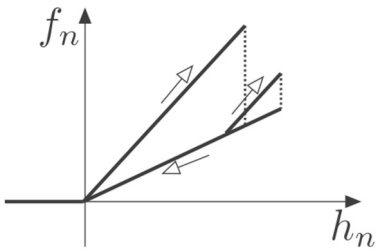



**Fig. 1** A sketch of the contact-or-collision force law in the normal direction

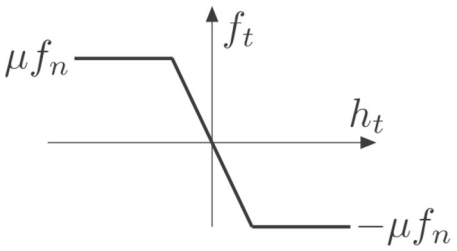



**Fig. 2** A sketch of the tangential elasto-plastic force law

increasing (compression loading), the increment of normal force is

$$\Delta f_n = k_n^{\text{load}} \Delta h_n \tag{1}$$

where $k_n^{\text{load}}$ is the loading stiffness coefficient. When the overlap is decreasing (unloading), the normal force is obtained using

$$f_n = k_n^{\text{unload}} h_n \tag{2}$$

where $k_n^{\text{unload}}$ is the unloading stiffness coefficient and $h_n$ is the overlap. This law is sketched in Fig. 1, where force jumps can be noticed at unloads. Such a jump sounds physically inconsistent; however, it is not an issue in our application context. The clear advantage of this law is the control that can be achieved over the amount of restituted energy in the normal direction, which corresponds to the surface area of a loop in the $f_n$–$h_n$ space. It is possible, for a touch-and-go collision, to express the energy restituted $e_n^2$ from the loading and unloading stiffnesses:

$$e_n^2 = \frac{k_n^{\text{unload}}}{k_n^{\text{load}}} \tag{3}$$

where $e_n$ is just the velocity-restitution coefficient sometimes used in trajectory analysis simulations.

For the tangential direction, an elastic incremental law was also employed, but with a plastic limit given by the Coulomb friction law $|f_t| <= \mu f_n$, where $\mu$ is the friction coefficient. This law is pictured in Fig. 2. The equations governing

the magnitude of the tangential force can be summarised as follows:

$$f_t = \min \left\{ \sum_{t_0}^{t} k_t \Delta h_t; \quad \mu f_n \right\} \tag{4}$$

where $k_t$ is the tangential stiffness, $t$ is the current time and $t_0$ is the time at which the contact initiated. The direction of each increment of the tangential force is set opposite to the sliding direction.

As already stated, the discrete element model employed in this paper uses realistic geometric shapes, by means of spheropolyhedra. This is actually a major concern in rheology that can be set in laboratory experiments. The relevance of the contact model and of the process needed to determine the parameters was estimated using laboratory tests and established by studying the simple rebounds of a small parallelepiped block on a rigid elastic support. This methodology was presented by Richefeu et al. [23], who tuned the dissipative parameters to adjust the energy balance during experimental collisions. Thanks to this process to determine the mechanical parameters, and taking into account complex shapes, the model was confronted to laboratory experiment made by Manzella and Labiouze [15], consisting of a small-scale rock avalanche starting from the release until the granular mass stops. In these experiments, the granular mass made of small clay bricks was placed inside a container on a steep slope (45°). At a given time, the lower wall of the container was removed to initiate the flow, and the mass subsequently stopped on a horizontal surface. After calibrating the parameters, this approach has successfully simulated the collective behaviour of the small brick mass (especially concerning the shape of the deposit and the type of flow) without retrospective analysis. Given the satisfactory correlation between the numerical model and the experiment, we chose this application to support this paper. Additionally to this validation process, sensitivity analyses with different block shapes and/or slope geometries have been done by Mollon et al. [19]. The resulting analysis is referred to later in this document to support the results of our study.

## 3 Material point method

The material point method (MPM) is a numerical method for the solution of problems in continuum mechanics that evolved from the particle-in-cell method [5,6,12,25]. The method solves the variational form of the conservation of momentum by discretising the continuum into material points and using a background Eulerian grid. The conservation of mass during the simulations is satisfied since the mass remains unchanged. A background grid is used to project the information carried by the material points and solve the equations of motion. This solutions found in the mesh are used to update the information contained in the material points. This interpolation/extrapolation between the mesh and the material points is done using shape functions. The MPM code that we used for this study is an enhanced MPM implementation that includes features such as the splitting of the material points once the deformation of individual volumes becomes too large, the use of DEM-like boundary conditions based on overlapping between the material point volume and the boundary and the use of higher-order shape functions to reduce errors related to cell-crossing instabilities.

### 3.1 Conservation equations

In the material point method, since we are modelling a continuous material undergoing deformations under prescribed forces and initial conditions, we must satisfy the conservation of mass and the conservation of momentum. The conservation of mass is achieved implicitly since a single mass value is given to each of the material points at the beginning of a simulation, and it remains unchanged.

We now consider a body $\Omega$, in which the conservation of mass is governed by:

$$\frac{\partial \rho(\boldsymbol{x},\ t)}{\partial t} + \nabla \cdot \Big( \rho(\boldsymbol{x},\ t)\ \boldsymbol{v}(\boldsymbol{x},\ t) \Big) = 0 \tag{5}$$

where $\rho$ represents the material density and $\boldsymbol{v}$ refers to the velocity at position $\boldsymbol{x}$ and time $t$. $\nabla$ is the gradient operator. We also have in terms of infinitesimal strain theory that the conservation of linear momentum is given by:

$$\rho \boldsymbol{a}(\boldsymbol{x},\ t) = \nabla \cdot \boldsymbol{\sigma}(\boldsymbol{x},\ t) + \rho \boldsymbol{b}(\boldsymbol{x},\ t) \tag{6}$$

in which $\boldsymbol{\sigma}$ is the Cauchy stress tensor, $\boldsymbol{b}$ are the body forces and $\boldsymbol{a}$ is the acceleration. Given that the Cauchy stress tensor is symmetric, the conservation of the angular momentum is guaranteed. The equation of conservation of linear momentum can be written in a weak form as follows:

$$\begin{aligned} \int_{\Omega} \rho \boldsymbol{a} \cdot \tilde{\boldsymbol{v}}\ \mathrm{d}\Omega = &- \int_{\Omega} \boldsymbol{\sigma} : \nabla \tilde{\boldsymbol{v}}\ \mathrm{d}\Omega \\ &+ \int_{\Omega} \rho \boldsymbol{b} \cdot \tilde{\boldsymbol{v}}\ \mathrm{d}\Omega + \int_{\partial\Omega} \boldsymbol{\tau} \cdot \tilde{\boldsymbol{v}}\ \mathrm{d}\partial\Omega \end{aligned} \tag{7}$$

in which $\tilde{\boldsymbol{v}}$ is a test function, and $\boldsymbol{\tau}$ are the boundary forces.

We emphasise here that the previous relations apply only for infinitesimal transformations. For large deformations, the infinitesimal strains are cumulated, but no finite strain theory is actually employed.

### 3.2 Discretisation of the MPM

Using the weak form of the conservation equations, we can now proceed to obtain the discretised equations that constitute the material point method [26]. In this part, we will use the subscript $p$ to refer to the material points, while the subscript $i$ will be used to refer to the background grid nodes. The density, stress and acceleration fields are discretised into material points by using appropriate shape functions $N_{ip}$, as shown below:

$$\rho_i(\boldsymbol{x}) = \sum_p \frac{m_p N_{ip}(\boldsymbol{x})}{V_p} \tag{8}$$

$$\boldsymbol{\sigma}_i(\boldsymbol{x}) = \sum_p \boldsymbol{\sigma_p} N_{ip}(\boldsymbol{x}) \tag{9}$$

$$\rho_i(\boldsymbol{x})\boldsymbol{a}_i(\boldsymbol{x}) = \sum_p \frac{\dot{\boldsymbol{q}}_p N_{ip}(\boldsymbol{x})}{V_p} \tag{10}$$

in which $m_p$ and $V_p$ are the mass and the volume associated with the material point $p$, respectively, and $\dot{\boldsymbol{q}}_p$ is its rate of momentum. The shape functions $N_{ip}$ are required to be a fraction of unity.

By substituting all the previous equations into the variational form of the conservation of momentum, and using $N$ as the test function, the discrete governing equations are found:

$$\boldsymbol{f}_i^{\text{ext}} - \boldsymbol{f}_i^{\text{int}} = \dot{\boldsymbol{q}}_i \tag{11}$$

in which the external forces, comprising those related to the surface and the volume, are:

$$\boldsymbol{f}_i^{\text{ext}} = \int_{\partial\Omega} \boldsymbol{\tau} N_{ip} \mathrm{d}\Omega + \sum_p m_p \boldsymbol{b} N_{ip} \tag{12}$$

The DEM-like forces due to boundary conditions are included in the first term. The same force laws as described in Sect. 2 are used to compute $\boldsymbol{\tau}$, which includes the normal and tangential contact forces at the level of the material points. This is performed by using an incremental procedure that updates the contact forces (see Sect. 2) by considering increments of normal and tangential relative displacements between a disc of diameter $\sqrt{V_p}$ surrounding the material points and the boundary condition. Our choice of contact law implies that the soil response is limited to a restitution-monitored elasticity along with Coulomb friction, but no plasticity is taken into consideration for the normal direction—which is reasonable for the laboratory experiments that we are dealing with in this paper. These boundary conditions can be used to create individual obstacles (fixed or free to move) which can be treated as DEM elements, and the classical boundary conditions of MPM (i.e., velocities reset at some nodes) can thus be replaced by these obstacle elements. This coupling between MPM and DEM was implemented by setting some mass properties to the obstacles, and then by integrating their motion. The explicit integration scheme of the DEM (velocity Verlet algorithm) is thus embedded within the explicit integration scheme of the MPM (modified Lagrangian algorithm) by sharing the same time, but not necessarily the same time increments. As a result, some rigid elements can move through space as they interact with material points and other discrete elements.

Back to Eq. (11), the internal forces are:

$$\boldsymbol{f}_i^{\text{int}} = \sum_p V_p \boldsymbol{\sigma}_p \cdot \boldsymbol{\nabla} N_{ip} \tag{13}$$

and the rate of momentum is:

$$\dot{\boldsymbol{q}}_i = \sum_p \dot{\boldsymbol{q}}_p N_{ip}. \tag{14}$$

### 3.3 Scheme of the explicit solutions

Our code is an explicit implementation of the MPM that uses the modified Lagrangian algorithm, explained in Fig. 3. In short, we start with a clean background grid to which we interpolate the mass and the velocities of the material points at the current time. Consequently, forces are calculated on

1: **Discard** the previous grid
2: **Compute** the shape functions $N_{ip}$ and their gradients $\boldsymbol{\nabla} N_{ip}$ as a function of the current position $\boldsymbol{x}_p$ of the MP
3: **Compute** the lumped nodal mass $m_i = \sum_p m_p N_{ip}$
4: **Map** the MP velocities $(\boldsymbol{v}_p^k)$ to the nodes $(\boldsymbol{v}_i^k)$ as momentum $(\boldsymbol{q}_i^k = m_i \boldsymbol{v}_i^k)$
5: **Compute** nodal forces:
$\boldsymbol{f}_i^{\text{int}} = -\sum_p V_p(\boldsymbol{\sigma}_p \cdot \boldsymbol{\nabla} N_{ip})$
$\boldsymbol{f}_i^{\text{ext}} = \sum_p m_p \boldsymbol{g} N_{ip}$
$\boldsymbol{f}_i^{\text{obs}} = \sum_p \boldsymbol{f}_p^{obs} N_{ip}$
6: **Compute** rate of momentum $(\dot{\boldsymbol{q}}_i)$ in the nodes as the sum of all nodal forces
7: **Map** accelerations $(\dot{\boldsymbol{v}}_p)$
8: **Update** MP velocities $\boldsymbol{v}_p^{k+1} \leftarrow \boldsymbol{v}_p^k + \dot{\boldsymbol{v}}_p \Delta t$
9: **Map** momentum $(\boldsymbol{q}_i)$
10: **Update** nodal momentum $\boldsymbol{q}_i^{k+1} \leftarrow \boldsymbol{q}_i^k + \boldsymbol{q}_i$
11: **Compute** the strain increment from nodal velocities
$\Delta\boldsymbol{\varepsilon}_p = \Delta t \sum_i \frac{1}{2}(\boldsymbol{v}_i^{k+1} \otimes \boldsymbol{\nabla} N_{ip} + \boldsymbol{\nabla} N_{ip} \otimes \boldsymbol{v}_i^{k+1})$
12: **Compute** $\Delta\boldsymbol{\sigma}_p$ using a constitutive model, and update the stress $\boldsymbol{\sigma}_p$
13: **Update** MP positions $\boldsymbol{x}_p^{k+1} \leftarrow \boldsymbol{x}_p^k + \boldsymbol{v}_p \Delta t$
14: **Update** MP volume and density using volumetric strain

**Fig. 3** Modified Lagrangian Algorithm

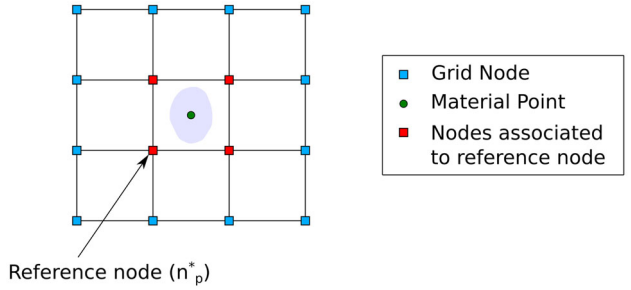



**Fig. 4** Structured background grid. Reference node and its associated nodes

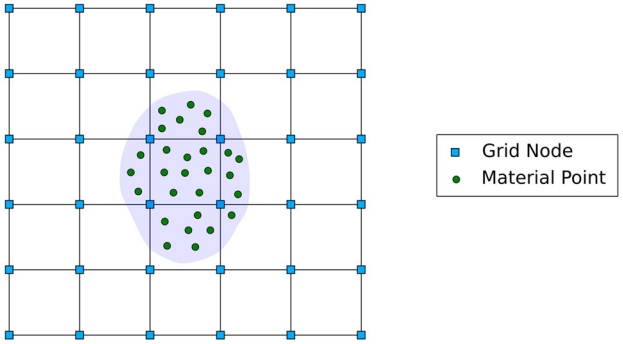



**Fig. 5** Continuum discretisation

the grid nodes (internal, external and obstacle forces), with which a rate of momentum is found. This rate of momentum allows us to update the material point velocities. We now update the momentum on the grid nodes using the new MP velocities. At this point, the nodal momentum is updated and the strains are computed using the nodal velocities, which are subsequently used to calculate stresses using an appropriate constitutive law. At last, the MP positions as well as their volume and density are updated, thus concluding a single step.

### 3.4 Background grid

The background grid in the material point method is represented in the Eulerian description, unlike the material points which are in the Lagrangian description. This means that the continuum moves and deforms freely without deforming the background grid. This is one of the main differences with the Lagrangian finite element method, in which both the grid and the continuum are represented in the Lagrangian description, which in cases of large deformations can cause severe mesh distortion, thus producing errors when interpolating between the grid and the Gaussian points unless remeshing is used.

The background grid in the MPM is composed of nodes as shown in Fig. 4. It is used as a computational scratchpad only, since at the end of every computational cycle all the information carried by the nodes is set to zero. This means that at the beginning of each cycle, the information used by the nodes will always be provided by the material points. Information like forces and velocities, among others, is transferred between the grid nodes and the material points by means of shape functions. Higher-order shape functions are preferred in order to reduce cell-crossing instabilities.

In the MPM, it is very common to use a structured grid. It provides great ease when finding the nodes associated with a material point at a certain time. In 2D, a reference node can be easily found using the following equation:

$$n_p^\star = \text{trunc}\left(\frac{x_p - x_{\min}}{\Delta x}\right) + \text{trunc}\left(\frac{y_p - y_{\min}}{\Delta y}\right) N_x \qquad (15)$$

which will have the appropriate nodes associated with it in order to transfer information from the material points to the appropriate nodes (Fig. 4). $x_{\min}$ and $y_{\min}$ refer to the minimum grid nodes coordinates, $x_p$ and $y_p$ are the position coordinates of the material point, $N_x$ is the number of nodes in the $x$ direction and $\Delta x$ and $\Delta y$ are the regular spacing of nodes in the $x$ and $y$ directions, respectively. It is important to say that the nodes associated with each reference node are found at the beginning of a simulation and remain the same throughout the simulation.

### 3.5 Continuum discretisation and shape functions

The discretisation of a continuum body is a step that is made at the beginning of the simulation (Fig. 5). The domain is divided into different material points with their masses lumped at single positions. The continuity of the domain is achieved with the Eulerian grid, in which the momentum equations are solved. As said before, the material points (Lagrangian description) carry all the information, while the values in the Eulerian grid nodes are set to zero at the end of every time step.

Shape functions allow us to interpolate information between the material points and the nodes, and vice versa. They provide us with a proper weight relative to each of the nodes surrounding the material point, so that information can be distributed evenly depending on the distance of each node from the material point position. It is required for the shape functions to be a partition of unity. During the initial stages of development of our MPM code, piecewise-linear basis functions were utilised. These types of shape functions are commonly used given that they are easy to implement. However, simulations tend to become unstable when very large deformations take place. It has been shown, in Bardenhagen and Kober [2], that low-order shape function (e.g., $C_0$) is the main cause of grid cell-crossing instabilities. As described by Bardenhagen, unexpected computational artefacts appear, especially when computing the internal forces. We deemed it necessary to include higher-order shape func-

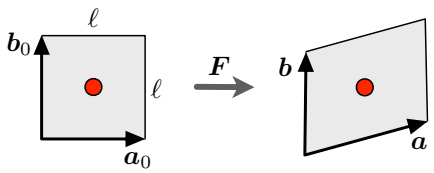



**Fig. 6** Transformation of a box by applying the deformation gradient tensor $\boldsymbol{F}$

tions (cubic B-splines) in our code in order to reduce errors related to this type of instability. The trade-off is, however, an increase in computational time since more grid nodes are involved for every material point.

## 3.6 Volume surrounding each material point

### 3.6.1 Deformation

One of the numerical aspects to be taken into account when using the material point method is the fact that the volume occupied by a material point is going to deform beyond acceptable values. It means that the set of material points needs to remain as consistent as possible when large deformations take place. This can be achieved by adding some new material points where spaces are being created within the material (splitting), and by removing some points in zones where they are too numerous (merging).

In the MPM, the volume associated with a material point is initially defined as a square, with the position of the material point acting as its centre and having a side length $\ell = \sqrt{V}$. This square depicts the volume that the material point represents. At the beginning, as illustrated in Fig. 6, it can be defined with two vectors $\boldsymbol{a}_0$ and $\boldsymbol{b}_0$ such that

$$\boldsymbol{a}_0 = \begin{pmatrix} \ell \\ 0 \end{pmatrix} \quad \text{and} \quad \boldsymbol{b}_0 = \begin{pmatrix} 0 \\ \ell \end{pmatrix} \tag{16}$$

When the material flows, the constituting material points deform, and their deformation can be expressed by means of the *deformation gradient tensor* $\boldsymbol{F}$ which is an operator that transforms the initial box into the current one. This is illustrated in Fig. 6. Formally, the vector $\boldsymbol{a}_0$ will be transformed into a vector $\boldsymbol{a}$, and the vector $\boldsymbol{b}_0$ will be transformed into a vector $\boldsymbol{b}$:

$$\boldsymbol{a} = \boldsymbol{F} \cdot \boldsymbol{a}_0 \quad \text{and} \quad \boldsymbol{b} = \boldsymbol{F} \cdot \boldsymbol{b}_0 \tag{17}$$

where $\boldsymbol{F}$ is expressed as

$$\boldsymbol{F} = \begin{bmatrix} F_{xx} & F_{xy} \\ F_{yx} & F_{yy} \end{bmatrix} \tag{18}$$

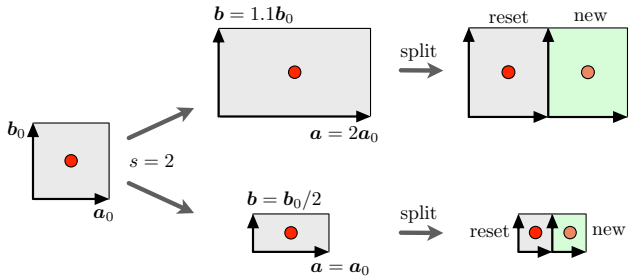



**Fig. 7** Scheme of the splitting principle for $s = 2$ illustrated with no tilt of the box and for the direction of $\boldsymbol{a}$; (top row) case of splitting due to $|\boldsymbol{a}|/|\boldsymbol{a}_0| = s$, (bottom row) case of splitting due to $|\boldsymbol{a}|/|\boldsymbol{b}| = s$

As the material starts to deform, the deformation gradient tensor is updated at each time step using the following relation:

$$\boldsymbol{F}^{k+1} = \Delta\boldsymbol{F}^{k+1} \cdot \boldsymbol{F}^{k} \tag{19}$$

with

$$\Delta\boldsymbol{F}^{k+1} = \boldsymbol{I} + \Delta t \sum_{N} \boldsymbol{v_n}^{k} \cdot \nabla N_p \tag{20}$$

where $N$ represents the nodes that are associated with the material point in its current position, and $\boldsymbol{I}$ is the identity tensor.

### 3.6.2 Splitting

The splitting algorithm consists in cutting a parallelogram spanned by $\boldsymbol{a} \times \boldsymbol{b}$ along either $\boldsymbol{a}$ or $\boldsymbol{b}$ into two identical smaller parallelograms. The two resulting material points have half the mass and volume of the original MP. From the numerical point of view, the first sub-parallelogram is the original one for which $\boldsymbol{F}$ has been reset, as shown in Fig. 7. The second sub-parallelogram is a new one, but it inherits all the properties—except the mass and the volume—held by the previous material point; in particular, it shares the initial box $\boldsymbol{a}_0 \times \boldsymbol{b}_0$ with the original parallelogram.

Let's now see how the criteria for splitting are expressed. The splitting along $\boldsymbol{a}$ is performed (1) if $\boldsymbol{a}$ is longer than $\boldsymbol{a}_0$ by a factor $s$ ($|\boldsymbol{a}|/|\boldsymbol{a}_0| \geq s$), or (2) if $\boldsymbol{a}$ is longer than $\boldsymbol{b}$ by the same factor $s$ ($|\boldsymbol{a}|/|\boldsymbol{b}| \geq s$). By using Eq. 17, it is easy to base the splitting criteria along $\boldsymbol{a}$ on the components of the deformation gradient tensor $\boldsymbol{F}$:

$$(F_{xx})^2 + (F_{yx})^2 \geq s \quad \text{or} \quad \frac{(F_{xx})^2 + (F_{yx})^2}{(F_{xy})^2 + (F_{yy})^2} \geq s \tag{21}$$

For splitting along the direction of $\boldsymbol{b}$, the equivalent criteria are (1) $|\boldsymbol{b}|/|\boldsymbol{b}_0| \geq s$ and (2) $|\boldsymbol{b}|/|\boldsymbol{a}| \geq s$, which correspond to the following criteria in terms of $\boldsymbol{F}$:

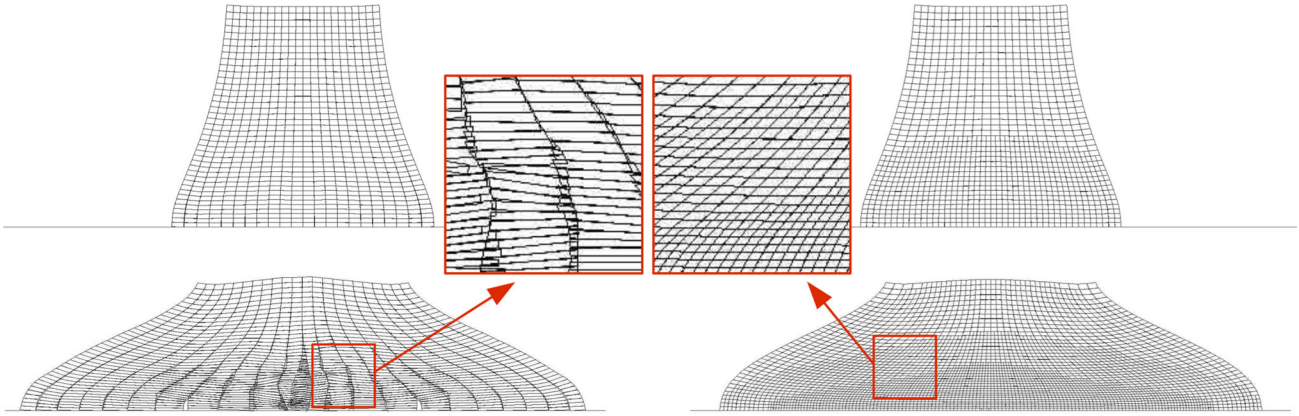


**Fig. 8** Slump test without splitting (left) and by using the splitting strategy (right)

$$(F_{xy})^2 + (F_{yy})^2 \geq s \quad \text{or} \quad \frac{(F_{xy})^2 + (F_{yy})^2}{(F_{xx})^2 + (F_{yx})^2} \geq s \tag{22}$$

This method has proved to be convenient when dealing with large box deformations in the directions of $\boldsymbol{a}$ and $\boldsymbol{b}$. However, deformations due to shear are not dealt with and should be a subject of study if this is of interest. To demonstrate the benefit of the splitting strategy, Fig. 8 shows two snapshots of simulations of a concrete column flow (slump test) in which an elasto-plastic constitutive model is used. The initial shape of the column was rectangular. In Fig. 8, the image on the left is a regular simulation, while the one on the right has been obtained using the splitting technique. When looking at the two zoomed regions, it is clear how consistency of the volume is better preserved, which results in a simulation in which overlaps of individual volumes are significantly restricted.

## 3.7 Mohr-Coulomb constitutive relation

Given the continuum nature of the MPM, constitutive relations are used to represent the behaviour of the material. The method uses the velocities in the nodes to compute the rate of deformation of a material point, which is necessary for the constitutive relation to determine the equivalent stresses. In the field of geomechanics, materials are modelled as history-dependent media, as is the case when using elasto-plastic constitutive relations. For the purposes of this paper, an elasto-plastic constitutive law (Mohr-Coulomb) was used for the sake of simplicity and to evaluate its relevance regarding its application to granular flows.

### 3.7.1 Yield criterion

The Mohr-Coulomb criterion (Fig. 9) implemented in our code is commonly used to describe the behaviour of geomaterials. This criterion takes into account the fact that the yield

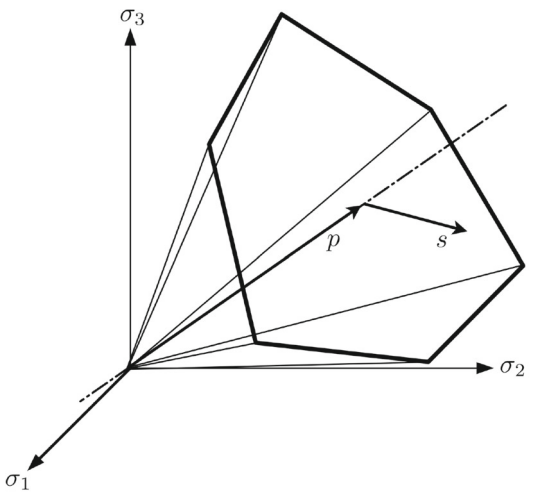



**Fig. 9** Mohr-Coulomb yield criterion plotted in the principal stress frame [7]. For a given pressure $p$, the stress state expresses as a non-spherical stress $s$ in the deviatoric plane. In this plane, the yield surface is shaped into a hexagon with six singularities where the normal to the surface in not uniquely defined. Another singularity appears for $p = s = 0$

stress depends on the hydrostatic component of the stress tensor. A return algorithm is used to fulfil the yield condition, and in this case, since the Mohr-Coulomb criterion is linear, only one step is necessary to return to the surface (if the plastic potential is also linear). Given that the Mohr-Coulomb criterion has certain regions such as intersections between planes which are discontinuous, care was taken in order to return to the appropriate region on the yield surface.

In general, the Mohr-Coulomb criterion predicts that failure of the material takes place if the shear stress reaches a critical value, or mathematically [30]:

$$\tau = c + |\sigma| \tan \phi \tag{23}$$

The shear stress $\tau$ depends on the normal stress $\sigma$, the friction angle $\phi$ and the cohesion $c$.

Yields functions can be formulated in terms of principal stresses as:

$$f(\boldsymbol{\sigma}) = (\sigma_1 - \sigma_3) + (\sigma_1 + \sigma_3)\sin\phi - 2c\ \cos\phi = 0 \quad (24)$$

with the plastic potential being:

$$g(\boldsymbol{\sigma}) = (\sigma_1 - \sigma_3) + (\sigma_1 + \sigma_3)\sin\psi \quad (25)$$

where $\psi$ refers to the dilatancy angle.

### 3.7.2 Return algorithm

In computational plasticity, the procedure undertaken consists in applying small load increments (in order to approach the yield surface cautiously) and therefore obtaining respective strain increments. Initially, the stress states will be elastic ($f < 0$), yielding elastic strain increments $\mathrm{d}\boldsymbol{\varepsilon} = \mathrm{d}\boldsymbol{\varepsilon}^{\mathrm{e}}$. If the material continues to be loaded, a point will be reached in which the stress state will lie outside of the yield surface ($f > 0$). As it was mentioned before, this region is inadmissible and a solution to make the stress state return to the surface is required. To deal with this type of problem, a return algorithm can be implemented, making the stress state lie on the surface of the yield surface after the correction.

This algorithm begins by attempting elastic trial step ($\boldsymbol{\sigma}^{e\text{-trial}}$). This means that we assume at each step to have an elastic state of stress at first:

$$\boldsymbol{\sigma}^{\text{e-trial}} = \boldsymbol{\sigma}^{k} + \boldsymbol{D} \cdot \mathrm{d}\boldsymbol{\varepsilon} \quad (26)$$

where $\boldsymbol{D}$ represents the elastic tensor, and $\boldsymbol{\sigma}^{k}$ is the current state of stress.

At this point, we check whether the state of stress is inside the yield surface by using the yield function $f(\boldsymbol{\sigma}^{\text{e-trial}})$. If the elastic trial yields a value $f < 0$, the state of stress is indeed elastic. Thus:

$$\boldsymbol{\sigma}^{k+1} = \boldsymbol{\sigma}^{\text{e-trial}} \quad (27)$$

and no plastic calculation is involved.

However, if the elastic trial yields a value $f > 0$, the state of stress lies outside the yield surface, making it necessary to return it to the yield surface using the return algorithm. For this, it is necessary to find an appropriate stress increment ($\Delta\boldsymbol{\sigma}$) so that the stress state is returned to the surface of the yield surface (Fig. 10).

The basic equation for the return (i.e. for the stress increment) is found to be:

$$\Delta\boldsymbol{\sigma} = \boldsymbol{D} \cdot \Delta\boldsymbol{\varepsilon} - \Delta\lambda \boldsymbol{D} \cdot \left(\frac{\partial g}{\partial \boldsymbol{\sigma}}\right) \quad (28)$$

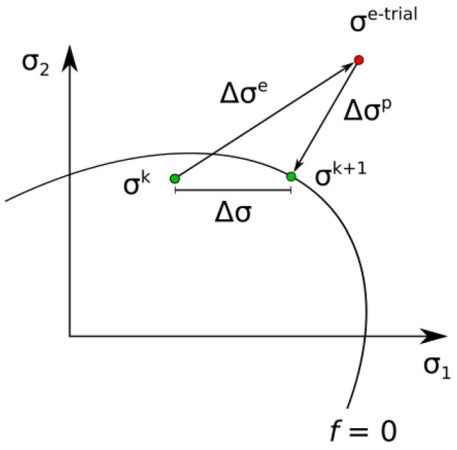



**Fig. 10** Return algorithm

or in other terms:

$$\Delta\boldsymbol{\sigma} = \Delta\boldsymbol{\sigma}^{\mathrm{e}} - \Delta\boldsymbol{\sigma}^{p} \quad (29)$$

The plastic corrector ($\Delta\boldsymbol{\sigma}^{p}$) is applied to the state of stress outside the surface, returning it to the yield surface. The plastic corrector represented by $\Delta\lambda\boldsymbol{D} \cdot (\partial g/\partial\boldsymbol{\sigma})$ is composed of a known plastic potential function representing the direction, and the plastic multiplier is defined as:

$$\Delta\lambda = \frac{f(\boldsymbol{\sigma}^{\text{e-trial}})}{\left(\frac{\partial f}{\partial \boldsymbol{\sigma}}\right)^{\mathrm{T}} \cdot \boldsymbol{D} \cdot \left(\frac{\partial g}{\partial \boldsymbol{\sigma}}\right)} \quad (30)$$

It must be noted that if associative plasticity is used, then a closed solution to the problem can be reached. In the case of non-associative plasticity, it is necessary to iterate using an appropriate numerical method, such as Newton's method, in order to fulfil the yield condition.

## 4 Applications

In this section, we compare two methods, the discrete element method and the material point method, in a series of simulations involving the flow of small bricks placed on a 45° slope which then transitions to a horizontal plane, as shown in Fig. 11. To provide some variability, we used different starting box sizes, basal friction coefficients, heights of release and shape of blocks in DEM. Different aspect ratios of the starting container ($0.246 \times 0.2 \times 0.2$ m$^3$ and $0.43 \times 0.2 \times 0.1$ m$^3$) were tested for different heights of release ($h = 0.4$ m, 0.8 m and 1.6 m) in order to vary the initial potential energy and the flow characteristics (homogeneous or non-homogeneous initial flow due to gravity effect and shape of the container). It must be noted that as the

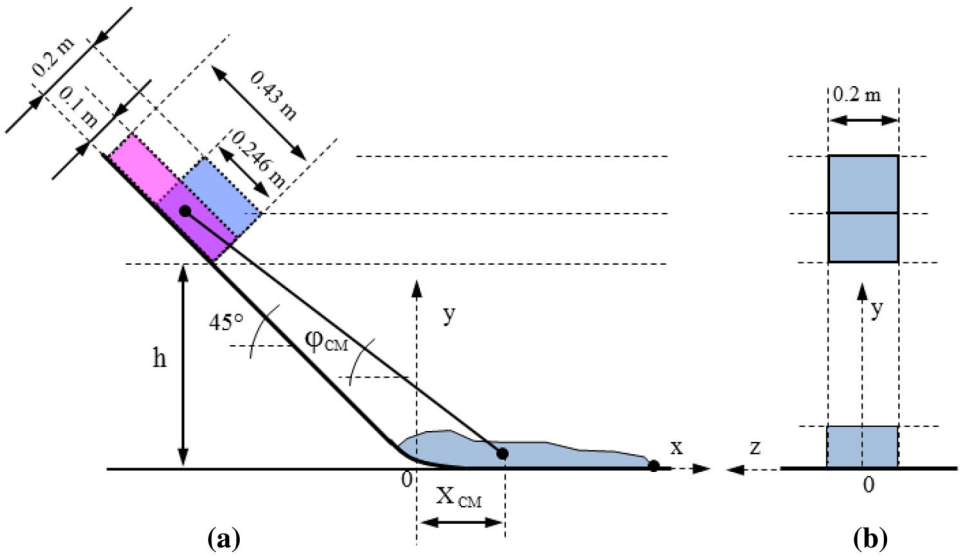



**Fig. 11** Simulation setup. The sizes of the two container boxes are shown together with the width of the channel, the slope angle, the varying initial height $h$ of the container, the runout distance $X_{CM}$ (equivalently related to the propagation angle $\varphi_{CM}$). The curved transition radius is 0.3 m

container shape varied, also did the centre of gravity. These numerical studies were done to reproduce the kinematics of granular avalanches and highlight the advantages and disadvantages of each type of numerical method. For this, various setups were introduced in the study, as is explained in the following section.

**Table 1** MPM internal elasto-plastic parameters

| | | | |
|---|---|---|---|
| Young's modulus | $E$ | 800 | kPa |
| Poisson's ratio | $\nu$ | 0.42 | – |
| Internal friction angle | $\varphi$ | 28.6 | ° |
| Cohesion | $c$ | $\sim 0$ | Pa |
| Dilatancy angle | $\psi$ | 0 | ° |

### 4.1 Geometry and mechanical parameters

Randomly packed blocks (cubes of $0.01 \times 0.01 \times 0.01$ m$^3$ or parallelepiped bricks of $0.02 \times 0.01 \times 0.005$ m$^3$) were used for the DEM simulations, while a continuum mass governed by an elasto-plastic law was considered for the MPM simulations. The starting container box was positioned on a 45° slope, ending at its toe with a smooth transition (radius 0.3 m) towards a horizontal plane where the mass stops after its propagation on the slope. The flow is initiated once the lower wall of the container is removed. DEM simulations are three-dimensional; the flow is thus canalised so that the comparison with the two-dimensional MPM simulations can be made. The canal width was set to 0.2 m to make the flow truly three-dimensional while limiting the number of elements. This width was chosen so that the ratio between the width and the size of a DEM particle was at least 10. For the comparison of the three-dimensional DEM simulations and the two-dimensional MPM simulations, an equivalent volumetric mass density was calculated for the MPM simulations in such a way that the total mass is the same as the DEM simulation ones, which depends on whether cubes or bricks were packed, as shown in Table 4.

The MPM elasto-plastic material flows according to the Mohr-Coulomb law for which properties are listed in Table 1. The chosen parameters are those corresponding to a non-cohesive coarse granular material with a dilatancy angle equal to zero. As a first approximation, the internal friction angle $\varphi = 28.6°$ was set to the residual macroscopic friction angle obtained at large deformations when simulating a triaxial test using the DEM (with cubic elements). Since this friction angle is obtained assuming static loading, we do not expect to perfectly reproduce the macroscopic behaviour of the DEM material during flow (Fig. 12), but that will allow us to make a reasonable comparison between the two models.

For the MPM simulations, a rather fine-structured background mesh was chosen, 15 mm × 15 mm, while the material point size was 5 mm × 5 mm—which corresponds to nine material points per mesh element at the beginning of a simulation, before any splitting. Figure 13 shows the material points together with the background grid, when the mass is flowing over the curved section and starts to stop. The number of elements used in the DEM simulations was around 6000 (the number was varying depending on the container and block shapes), while for the MPM simulations around 300 material points were used.

The contact parameters governing the contact-or-collision law between the DEM elements are given in Table 2. These parameters are those established after the calibration process [23] needed to reproduce the experiment of Manzella [15]. Note that, here and in the following, a parameter superscripted with a star ($\star$) relates to the bulk material.

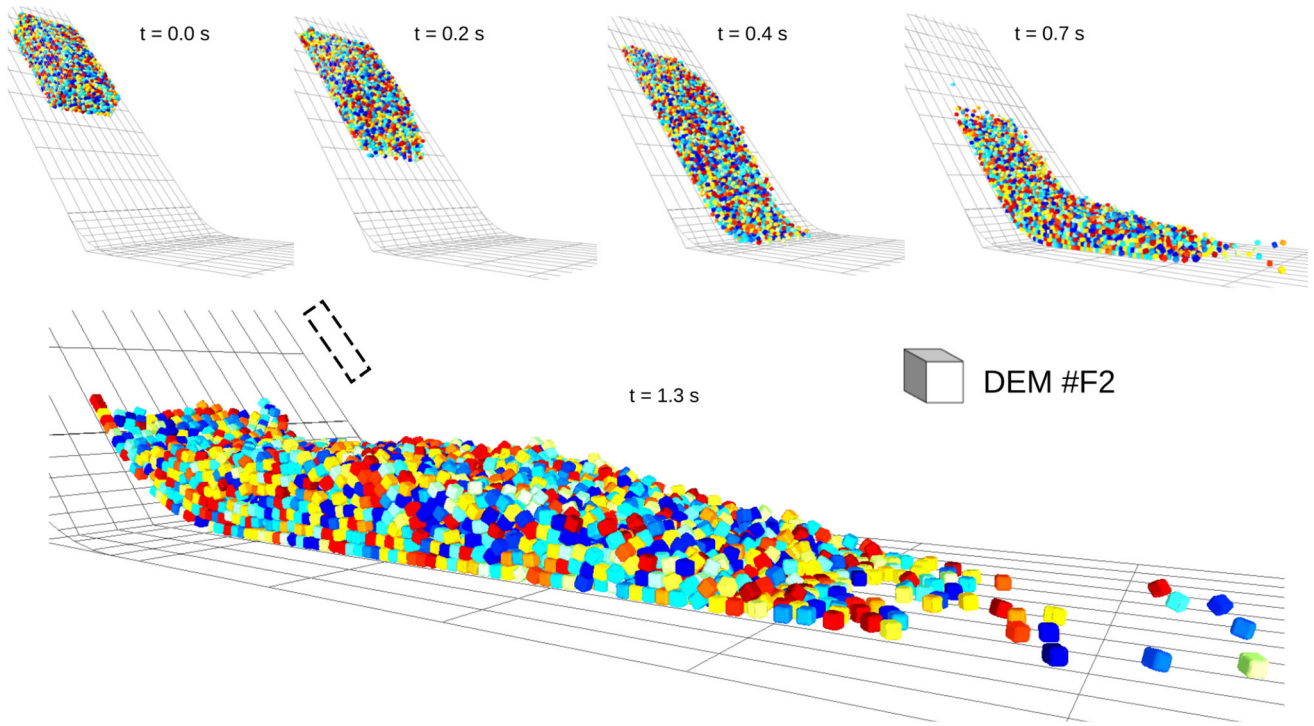



**Fig. 12** Example of a 3D DEM simulation used in the study displaying block velocities (#F2, $h = 0.8$ m)

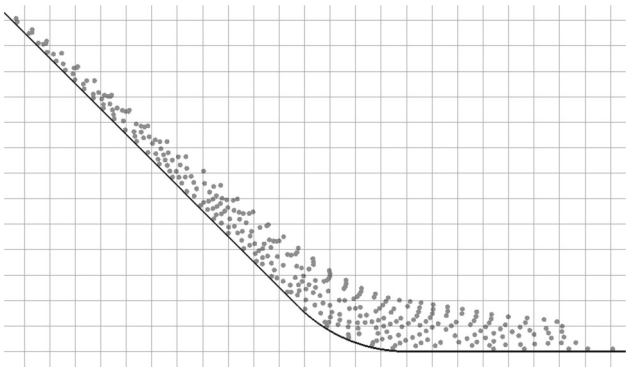


**Fig. 13** An example of MPM simulation where the material points can be viewed when they are passing the curved transition. The background grid, which is fixed, is also shown

**Table 2** DEM internal contact parameters (in between the blocks)

| | | | |
|---|---|---|---|
| Normal stiffness | $k_n^\star$ | $10^4$ | N/m |
| Stiffness ratio | $k_n^\star/k_t^\star$ | 2.5 | – |
| Friction coefficient | $\mu^\star$ | 0.7 | – |
| Energy restitution rate | $e_n^{\star 2}$ | 0.2 | – |

As mentioned previously, for the comparison of 3D-DEM with 2D-MPM propagations, the DEM mass flow had to be canalised. This was achieved by means of two vertical frictionless walls placed on both sides of the mass throughout the simulations.

**Table 3** Basal contact parameters for both MPM and DEM simulations

| | | | |
|---|---|---|---|
| Normal stiffness | $k_n$ | $10^6$ | (N/m) |
| Stiffness ratio | $k_n/k_t$ | 2 | – |
| Friction coefficient | $\mu$ | 0.3–0.7 | – |
| Energy restitution rate | $e_n^2$ | 0.2 | – |

The contact laws between the boundary conditions and MPM/DEM elements are those described previously. The related parameters can be found in Table 3. For the basal friction coefficients, we used three values in order to test its influence on the flow. We considered $\phi = 16.7°, 26.6°$ or $35°$, which correspond to the friction coefficients $\mu = 0.3, 0.5$ and 0.7. It must be noted that the first two friction coefficients at the base ($\mu$ =0.3 and 0.5) have a value lower than the internal friction coefficient $\tan(\varphi^\star) = \tan(28.6°) \simeq 0.545$ used for the Mohr-Coulomb elasto-plastic law, while the value $\mu = 0.7$ is greater.

In total, nine numerical simulations were performed for each value of the basal friction coefficients while varying other characteristics such as height of release, block shape (only for DEM) and container shape. Different block shapes in the DEM simulations provide different types of interactions between them, which end up having an influence on the type of flow produced, as well as the final outcome. The different setups (#A, #B and #C) that were used for

**Table 4** Sum-up of the different configurations

| | #A1/#D1/#G1 | #A2/#D2/#G2 | #A3/#D3/#G3 | #B1/#E1/#H1 | #B2/#E2/#H2 | #B3/#E3/#H3 | #C1/#F1/#I1 | #C2/#F2/#I2 | #C3/#F3/#I3 |
|---|---|---|---|---|---|---|---|---|---|
| Height of release (m) | 0.4 | 0.8 | 1.6 | 0.4 | 0.8 | 1.6 | 0.4 | 0.8 | 1.6 |
| Block Shape (DEM) |  |  |  |  |  |  |  |  |  |
| Body Shape |  |  |  |  |  |  |  |  |  |
| Container Density (kg/m3) | 1972 | | | 1577 | | | 1644 | | |

The DEM and MPM simulations are labelled with a hash character (#) followed by a letter (codifying the block and container shapes), and a number (codifying the height of release). Cases #A, #B and #C correspond to $\mu = 0.3$; cases #D, #E and #F to $\mu = 0.5$ and cases #G, #H and #I to $\mu = 0.7$

the simulations using a basal friction coefficient $\mu = 0.3$ are summarised in Table 4. The geometric configurations for the other two basal friction coefficients ($\mu = 0.5$ and 0.7) are the same, while the nomenclature is #D, #E and #F for the configurations having a friction coefficient $\mu = 0.5$, and #G, #H and #I for those with a friction coefficient of $\mu = 0.7$. An example of one of the 3D-DEM simulations can be seen in Fig. 12 performed with a basal friction coefficient $\mu = 0.5$. We can observe the individual interactions of the blocks, and how they flow freely down the slope after the initial release. Once the final deposit starts to form, it is evident that some individual blocks travel much further due to the discontinuous approach of this method. An interesting phenomenon also occurs once the final deposit is formed, in which the blocks at the bottom are, for the most part, aligned with the horizontal surface and the vertical frictionless walls. Given the shape of the blocks, they tend to have a rolling motion as long as they are on the slope, but once they reach the horizontal surface, the sliding mechanism is favoured.

## 4.2 Partition of the energy dissipated

In order to calculate the energy dissipated during the flow evolution, we separated it into internal and external (normal and tangential) energy. For the simulations run using the material point method, the cumulated work $\mathcal{W}^\star(t)$ of the internal forces within the mass was calculated as

$$\mathcal{W}^\star(t) = \sum_p \int_0^t V_p(\tau)\Big(\boldsymbol{\sigma}(\tau) : \dot{\boldsymbol{\varepsilon}}(\tau)\Big)\mathrm{d}\tau \tag{31}$$

where $V_p$, $\boldsymbol{\sigma}$ and $\dot{\boldsymbol{\varepsilon}}$ are, respectively, the volume, the total stress and the total strain increment held by each material point $p$. Note that the index $p$ is not used here for $\boldsymbol{\sigma}$ and $\dot{\boldsymbol{\varepsilon}}$ to avoid any confusion with plastic terms. The quantity $\mathcal{W}^\star(t)$ is of interest because it nearly corresponds to the amount of energy dissipated at each moment of the flow. The difference being the energy stored in the contacts when they become persistent (mass at rest), which is small compared to $\mathcal{W}^\star$ at the end of the flow. In other words, the elastic strains are negligible when compared to the plastic ones.

Concerning the energy dissipation between the blocks (DEM) and at the boundaries (both DEM and MPM), the overall cumulated work was split into three contributions: (1) the cumulated work $\mathcal{W}_n$ of the normal forces (persistent contacts and collisions) at the base of the flow, (2) the cumulated work $\mathcal{W}_t$ of the tangential forces (friction) at the base of the flow and (3) the work $\mathcal{W}^\star$ of all internal actions in the flowing mass. For the DEM, the dissipation within the mass was simply obtained as the sum of cumulated works of contact forces between the blocks in the normal and tangential directions:

$$\mathcal{W}^\star(t) = \mathcal{W}^\star_{\mathrm{n}}(t) + \mathcal{W}^\star_{\mathrm{t}}(t) \tag{32}$$

with

$$\mathcal{W}^\star_{\mathrm{n}}(t) = \int_0^t f_n(\tau)\dot{u}_n(\tau)\mathrm{d}\tau \tag{33}$$

and

$$\mathcal{W}^\star_{\mathrm{t}}(t) = \int_0^t f_t(\tau)\dot{u}_t(\tau)\mathrm{d}\tau \tag{34}$$

where $\dot{u}_n$ and $\dot{u}_t$ are, respectively, the normal and tangential relative velocities between the blocks. One more time, we assume that the reversible forces are negligible with respect to the irreversible ones, which makes both $\mathcal{W}^\star_{\mathrm{n}}(t)$ and $\mathcal{W}^\star_{\mathrm{t}}(t)$ almost equal to the dissipated energy at any moment $t$.

## 4.3 Results of basal friction coefficient 0.3. cases #A, #B and #C

First, we considered a basal friction coefficient $\mu = 0.3$, which corresponds to an angle $\phi = 16.7°$. This low friction coefficient (when compared to the internal friction angle of 28.6°) enables the material to slide down the slope without generating high internal shear stress. This makes the internal

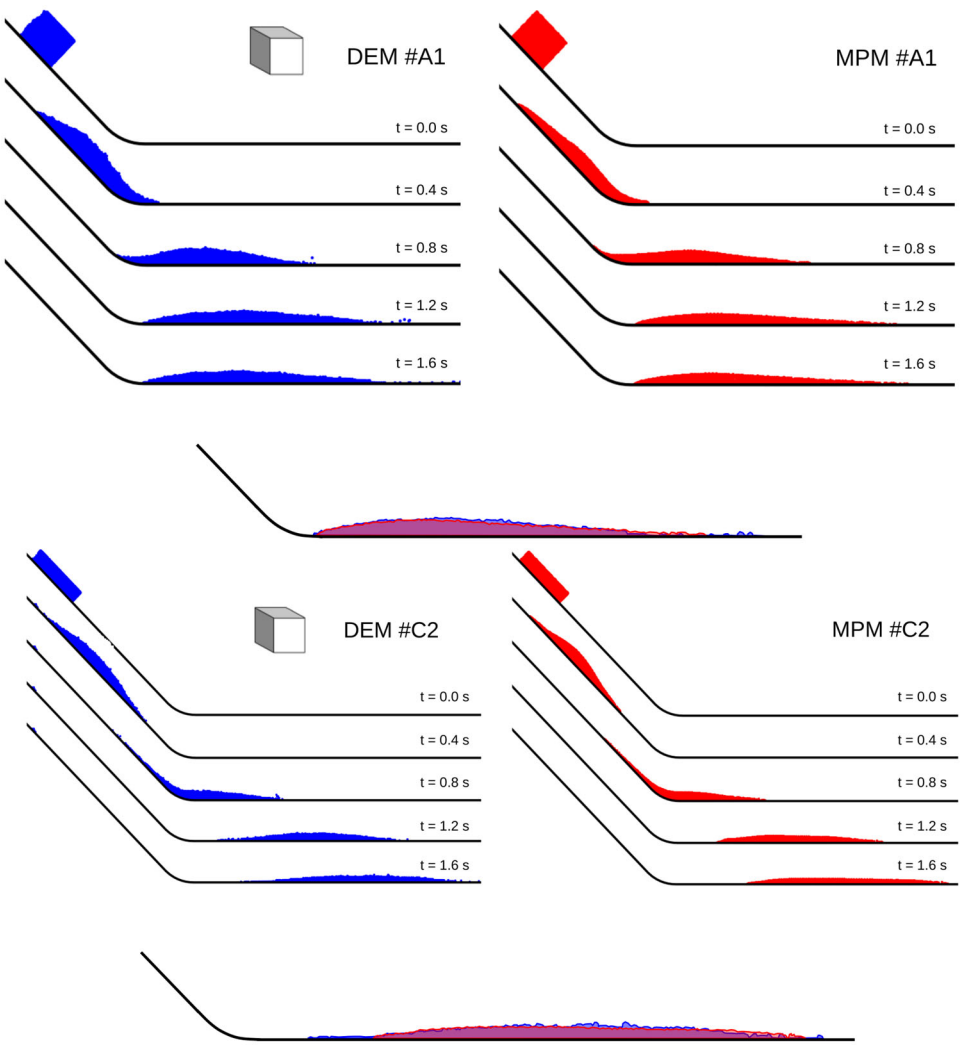



**Fig. 14** Kinematics for simulations #A1 ($h = 0.4$ m) and #C2 ($h = 0.8$ m) with DEM and MPM

dissipation mechanisms take a rather small part in the total dissipation as the material flows down the slope, as will be seen shortly.

Figure 14 displays two kinematic sequences for configurations #A1 ($\mu = 0.3$, released at 0.4 m, cubic blocks, cubic container) and #C2 ($\mu = 0.3$, released at 0.8 m, cubic blocks, elongated container) simulated using DEM and MPM. Overall, through the flow evolution, both methods seem to produce very close results. The deformation of the mass, the length from front to rear and the timing remain very similar. However, the curvature of the mass surface near the slope transition differs slightly between MPM and DEM simulations, and this is especially evident when using a cubic container. Moreover, the scattering of the blocks in the front of the deposit is completely missed by the MPM (a natural consequence of the continuity assumption). Apart from that, the main mismatch seems to appear at the very end, when the final heap is forming.

From a more quantitative point of view, Fig. 15 compares the centres of mass $X_{\mathrm{CM}}$ (bars) and the spreading lengths

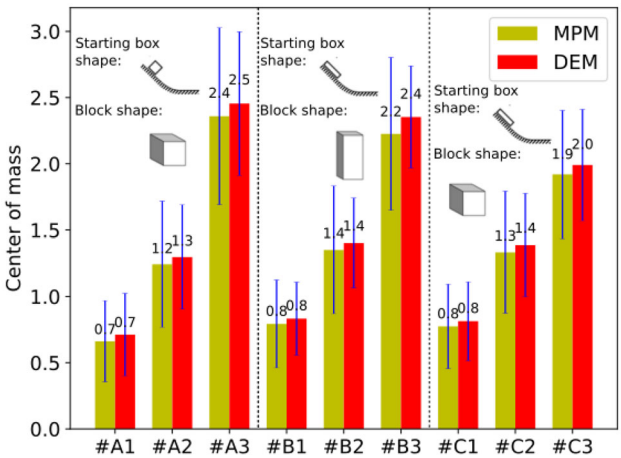



**Fig. 15** Runout distances and spreading lengths of the deposits for DEM and MPM simulations carried out with a basal friction coefficient $\mu = 0.3$

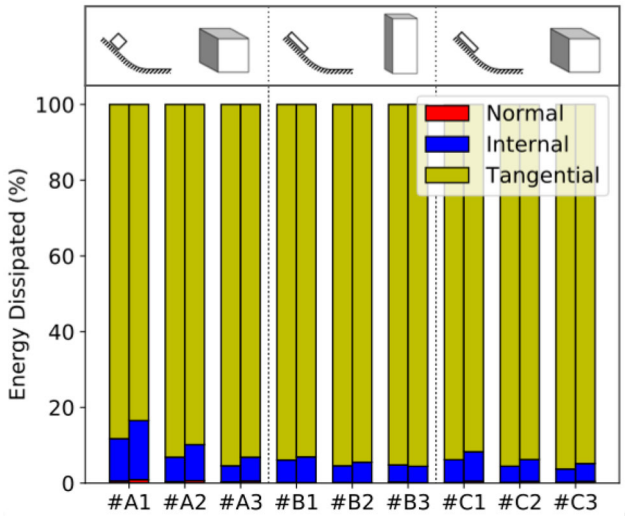



**Fig. 16** Total work involved in the flow for MPM (left bars) and DEM (right bars) simulation when the friction at the base is $\mu = 0.3$. This total work which is very close to the energy dissipated is partitioned into three terms: internal, basal collisions (normal) and basal friction (tangential)

$\sigma_{CM}$ (whiskers at the top of the bars) of the deposits for all simulations performed (#A, #B and #C). The bars on the left correspond to the MPM simulations, while the ones on the right relate to the DEM simulations. For most of the simulations with the current basal friction coefficient, the mass centres of the deposits using both methods remain very close.

Note that the small differences observed in Fig. 15 between MPM simulations #B and #C are simply the consequence of the differences in initial potential energy due to different mass densities (initially tuned to have the same total mass in DEM and MPM simulations) since the block shapes are not explicitly accounted for in the constitutive model used.

Taking a look at the partitions of energy dissipation during the simulations (Fig. 16), the MPM and DEM simulations are displayed in pairs (MPM on the left, DEM on the right) and the total energy dissipation is divided into collisions at the base ($\mathcal{W}_n$), friction at the base ($\mathcal{W}_t$) and internal ($\mathcal{W}^\star$) at the end of the simulations when the mass has stopped ($t = \infty$). There is a good match between the MPM and DEM results, and we can clearly observe that the driving means of dissipation are the friction at the base (tangential) for both DEM and MPM, while the internal energy plays a small part in the overall dissipation, especially during the initial deformation of the mass. Regarding the normal energy dissipated at the base by collisions, it can be neglected since its value is not representative.

In Fig. 16, however, the effect of the container shape, the block size and the height of release becomes more perceptible. For this given basal friction coefficient, the internal energy dissipated depends mostly on the container shape (for both DEM and MPM simulations). As an example, we can see that for cubic containers (#A), the internal energy dissipated is higher than that of the elongated containers (#B and #C). In fact, when the mass is released at the beginning of the simulation, it undergoes an initial deformation before achieving a fairly shallow shape, as seen in Fig. 14. This initial deformation constitutes the total internal energy dissipated, plotted in Fig. 16, since after this initial deformation the mass slides along the slope until reaching its stopping point. For the DEM simulations, the block shape also plays a part, as pointed out in [19]. In fact, the two block shapes employed in this study determine whether the elements are prone, or not, to rotation during the flow. This affects the deposit spread (as seen before), but also influences the amount of energy dissipated internally. Even if in this case the mass is mostly sliding, it can be seen that when using cubic elements the internal energy dissipated increases, which indicates some rolling within the material, as seen in simulations labelled #C.

In general for this given friction coefficient, the two methods generate very similar results in terms of centre of mass, spreading of the material and energy dissipated (normal, tangential and internal). Some characteristics such as the container shape and the type of blocks used in the DEM can generate some differences, but they remain very small. Additionally, qualitatively there is a rather good match between the two methods as seen in Fig. 14, not only in terms of shape but in terms of timing as well. In this particular situation where $\mu^\star$ is significantly lower than $\tan(\varphi)$ (that means that the internal dissipation phenomena are not predominant), the plastic constitutive law used (even roughly calibrated) seems properly adapted to reproduce the behaviour given by the DEM model.

### 4.4 Results of basal friction coefficient 0.5. cases #D, #E and #F

We now consider the basal friction coefficient $\mu = 0.5 \simeq \tan(26.6°)$. This friction is closer to the internal friction used for in the MPM simulations ($\varphi = 28.6°$) while remaining lower, which triggers a different response of the mass during the flow evolution. Due to the higher friction coefficient, the material undergoes much higher internal plastic strains, making it dissipate much more energy internally.

In Fig. 17, the kinematic sequences for configurations #D1 (cubic container, cubic blocks and released at 0.4 m) and #F2 (elongated container, cubic blocks and released at 0.8 m) are shown for DEM and MPM simulations. Overall, results are still correlated with a certain degree, but differences between the two methods start to surface and become more evident, especially when comparing the shape of the mass. Starting from the second frame in simulation #D1, the curvatures of the mass surfaces during flow clearly differ, and the whole

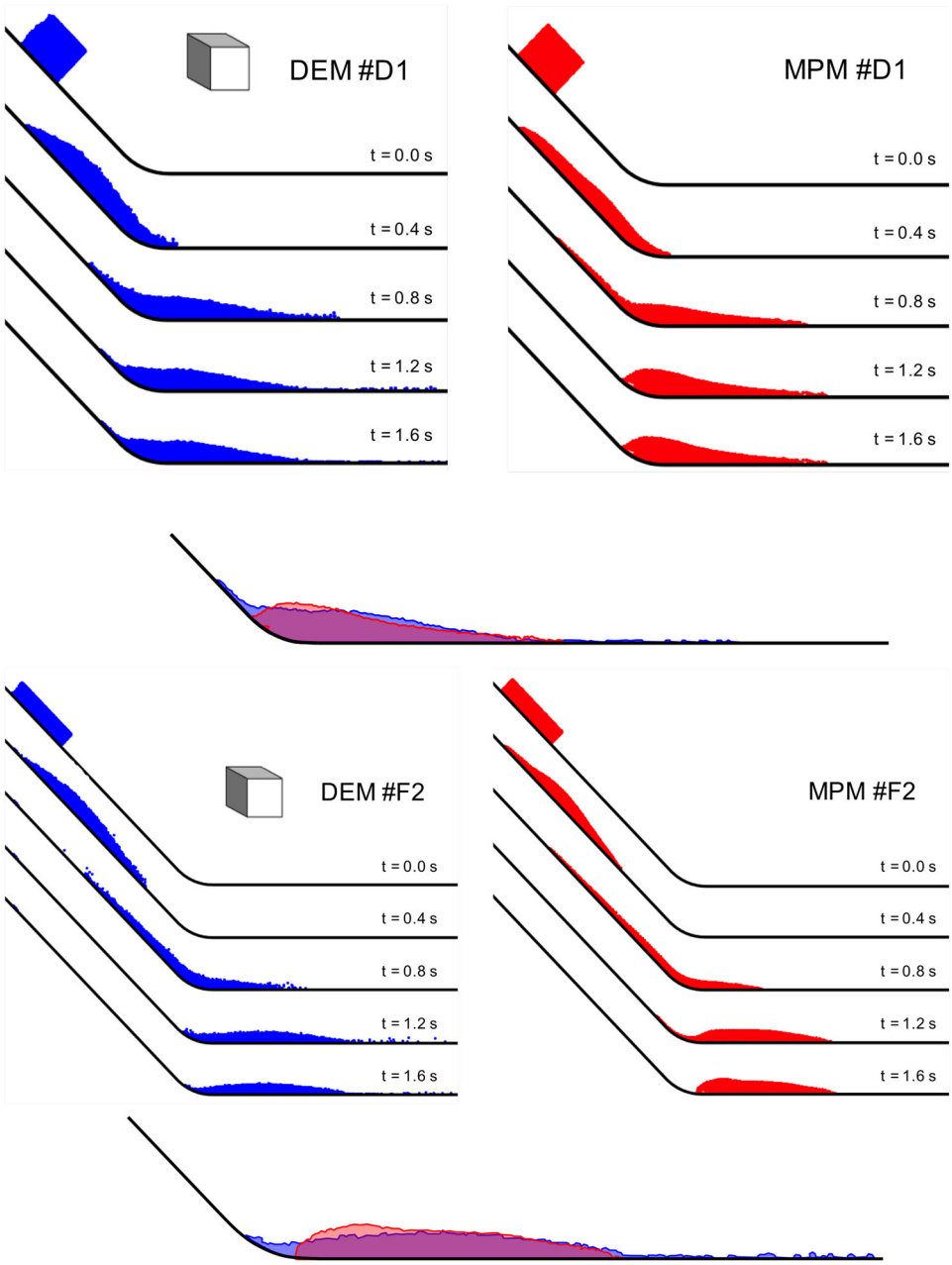



**Fig. 17** Kinematics for simulations #D1 ($h = 0.4$ m) and #F2 ($h = 0.8$ m) with DEM and MPM

mass spreads slightly less in the MPM simulations leading to different deposit shapes. Additionally, the flow evolution tends to be slightly delayed in the MPM simulations, which can be seen more clearly in the kinematic evolution of configuration #F2.

We turn now to Fig. 18, displaying a DEM/MPM comparison of the runout distances and the spreading of the deposits. This figure shows that proper correlations still take place in terms of runout distance, as was the case for the 0.3 basal friction coefficient, regardless of the container and block shape. However, with this higher basal friction ($\mu = 0.5$, Fig. 18), the runout distances are, as expected, smaller than those obtained previously ($\mu = 0.3$, Fig. 15). In terms of deposit spreading, some variation between the two methods starts to emerge (Fig. 18) due to the introduction of shearing mechanisms within the mass for MPM and between blocks for DEM. By noticing the variation of $\sigma_{CM}$, we can see how the shape of blocks, height of release, together with the container shape, become important. For cases #D, which is a cubic container and cubic blocks (prone to rotation), the $\sigma_{CM}$ tends to be larger for the DEM simulations. In cases #F, where the only difference is the box shape, the $\sigma_{CM}$ remains almost the same with DEM and MPM. At the opposite, for simulations labelled #E, since the blocks are brick-shaped, rotation

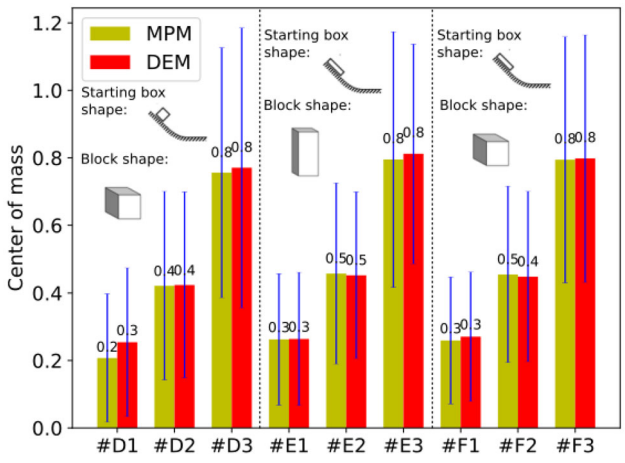



**Fig. 18** Runout distance and standard deviation for simulations with a basal friction coefficient of 0.5

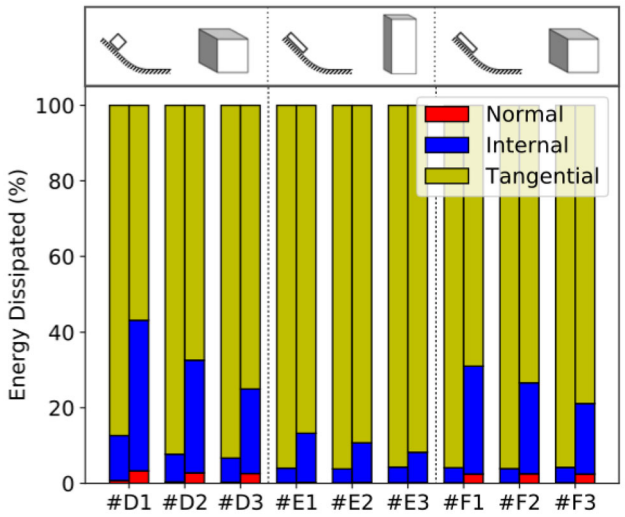



**Fig. 19** Total work involved in the flow for MPM (left bars) and DEM (right bars) simulations when the friction at the base is $\mu = 0.5$. The total work is partitioned into three terms: internal, basal collisions (normal) and basal friction (tangential)

is hindered, and the spread of the deposit remains lower than that of MPM in all cases.

Figure 19 complements what was mentioned about the sliding and rolling of the cubes for simulations labelled #D and #F. We can see how the amounts of internal energy dissipated are, compared to the basal frictional energy, evidently larger than those found for $\mu = 0.3$. Additionally, these values found using DEM are relatively larger than those of MPM, especially when the setups include cubic blocks, which roll and in turn dissipate much more energy internally than the MPM. It is important to highlight that the effect of the container size is seen in the amount of internal energy dissipated by relating the elongation of the container with the amount of internally dissipated energy (the thinner the container, the less plastic deformation develops within the mass).

Due to the fact that for these simulations the basal friction coefficient remained lower than the internal friction, we can see that the tangential energy is preserved as the main means of dissipation, even if the internal energy has a much larger value than for the previous basal friction coefficient. Finally, looking for cases #D and #F, both involving cubic blocks, it is worth noting that some collision dissipation at the base (work of normal forces at the base $\mathcal{W}_n$) occurs. This goes back to the "rolling effect" mentioned previously and indicates that some of the blocks are rolling beyond the initial mass length, impacting the slope directly, which also explains why the spreading of the deposit becomes larger.

By comparing the partition of energy dissipation for DEM and MPM when the basal friction changes from 0.3 to 0.5 (Figs. 16, 19, respectively), it can be observed that these partitions are rather the same for MPM; this is arguably due to the fact that the basal friction angle is lower than the internal friction angle and that the nature of the flow is not substantially changed. For DEM, an increase of the basal friction coefficient induces rotation of the cubic elements (#D and #F) which are more apt to rotate than elongated elements (#E). This induces a change in energy dissipation mode characterised mostly by an increase of dissipation within the mass (internal).

We can thus conclude that using a basal friction coefficient $\mu = 0.5$ provides different types of energy dissipation, which include more contact between the blocks and between the blocks and the base (DEM) and more energy dissipated plastically (MPM). However, dissipation due to friction between the material and the base is still present. In general, the final position of the centres of mass found using both methods still gives similar results, but in terms of energy dissipation mechanisms we start to have some major differences.

### 4.5 Results of basal friction coefficient 0.7. cases #G, #H and #I

In this final part of the study, we considered a basal friction coefficient $\mu = 0.7 \simeq \tan(35°)$. This time, unlike the previous two cases in which the basal friction coefficient remained lower than the internal friction coefficient, a definitely higher basal friction resistance is involved that favours shearing within the material.

In Fig. 20, we present the final deposits generated by simulations #G1 (cubic container, cubic blocks and released at 0.4 m) and #I2 (elongated container, cubic blocks and released at 0.8 m). This time, it is clear that the correlations previously seen between the two numerical models in cases with lower basal friction coefficients no longer exist. For simulations involving cubic elements, the centres of mass differ greatly, with the MPM having a much lower runout distance.

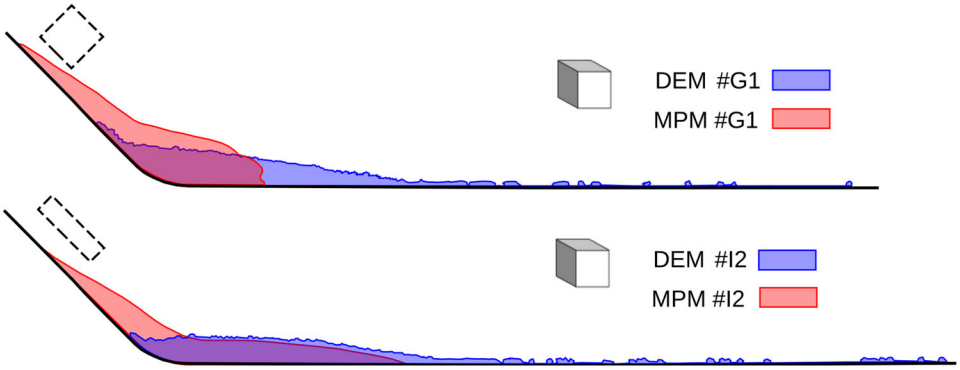



**Fig. 20** Deposits for simulations #G1 ($h = 0.4$ m) and #I2 ($h = 0.8$ m) with DEM and MPM

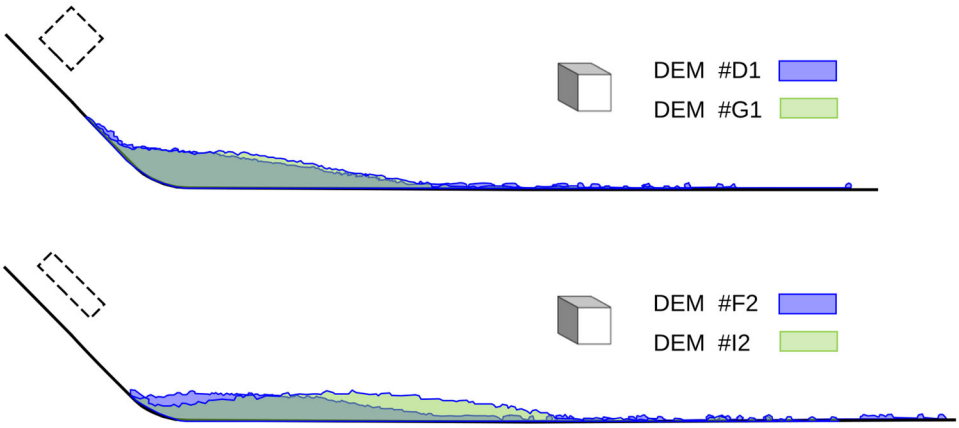



**Fig. 21** Comparison of the DEM deposits for different basal friction coefficients; $\mu = 0.5$ (blue) and $\mu = 0.7$ (green). Simulations #D1/#G1 ($h = 0.4$ m) and #F2/#I2 ($h = 0.8$ m). (Color figure online)

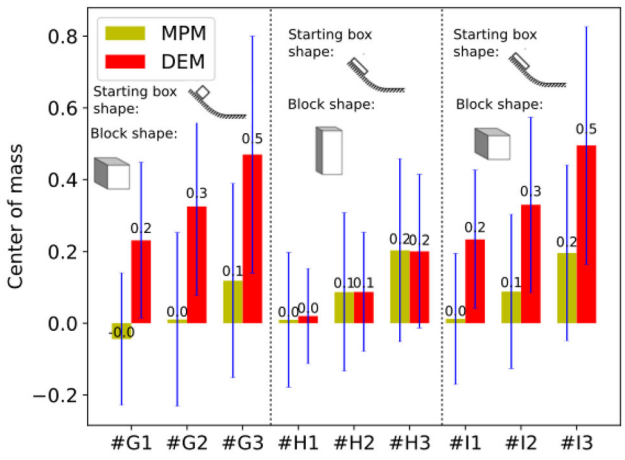



**Fig. 22** Runout distance and standard deviation for simulations with a basal friction coefficient of 0.7

Additionally, the spreading of the mass is in these cases much larger in the DEM simulations.

The consequences of an increase of the basal friction coefficient from $\mu = 0.5$ to $\mu = 0.7$ can be analysed regarding the Figs. 18 and 22 (runout distances and the spreading of the deposits), respectively. It appears that for MPM, an increase of the basal friction leads to important decreases of the runout distances since the mass is permanently in contact with the boundary. Similar trends can be seen for DEM simulations performed with elongated elements (#E ↔ #H) which preferentially tend to slide on the boundary. On the contrary, considering DEM simulations involving cubic elements, it seems that for the lower heights of release (#D1 ↔ #G1) and (#F1 ↔ #I1), the runout distances obtained with $\mu = 0.5$ and $\mu = 0.7$ are rather similar regardless of the values of the basal friction parameter. For higher heights of release, the increase of the basal friction angle in DEM with cubic elements induces a decrease of the runout distance. This is a consequence of complex dissipative mechanisms that can be captured by DEM and that cannot be reproduced by the MPM as explained in the following.

The difference in behaviour for cubic blocks is evidenced in Fig. 21, where only the friction coefficient is varied for two different configurations (#D1 ↔ #G1) and (#F2 ↔ #I2). One thing to highlight is that while on the slope, the DEM blocks tend to roll as described before, but once they reach the horizontal surface, they mostly tend to slide, which makes the basal friction mobilised again. On the slope, where blocks mostly rotate, an increase of the basal friction coefficient has almost no effect on the amount of basal dissipated energy and on the propagation distance. When cubic blocks arrive with a higher energy at the horizontal surface (higher heights of release), the sliding interaction between the blocks and the boundary becomes persistent, making the differences

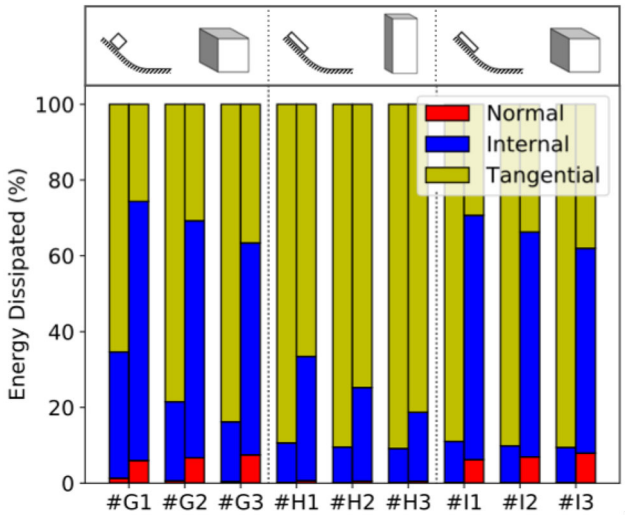



**Fig. 23** Total work involved in the flow for MPM (left bars) and DEM (right bars) simulations when the friction at the base is $\mu = 0.7$. The total work is partitioned into three terms: internal, basal collisions (normal) and basal friction (tangential)

between simulations with different basal friction coefficients more noticeable.

Comparison between MPM and DEM (Fig. 22) shows that in cases #G and #I, where cubic blocks used in the DEM simulations are more subjected to rolling, the runout distances differ drastically between the two models. On the other hand, cases labelled #H, in which the DEM blocks are brick-shaped, present a runout distance very similar to that of MPM, regardless of the height of release. However, a slightly larger spreading takes place in the MPM simulations. As was mentioned before, these brick-shaped blocks are not as prone to rolling, and overall the mass tends to slide down the slope. In terms of deposit spreading, since the propagation mechanism in cases labelled #G and #I is mainly rolling in the case of the DEM simulations, there are large differences when comparing the two methods.

We now turn to Fig. 23, which shows the different means of energy dissipation during the flow. Cases labelled #H, in which the MPM and DEM runout distances and deposit spreadings presented similar results (see Fig. 22), demonstrate that in both methods the principal means of dissipation is still frictional between the mass and the boundary. As mentioned in the previous paragraph when explaining cases labelled #G and #I (cubic elements), an increase in the basal friction does not lead to an increase of the tangential basal dissipated energy due to the rolling of the blocks on the slope. This can be seen in an increase of the internal dissipated energy, especially for lower heights of release for which blocks do not propagate on the horizontal plane. In addition, an increase in normal energy dissipated can be seen which is related to the constant rolling of the cubes and their collision with the surface, which means the blocks are rolling beyond the initial mass length.

Therefore, using this basal friction coefficient as an example, we can say that in order to have a better approximation to the complex behaviour shown by the DEM, the present elasto-plastic law should be improved. In addition, a law capable of better representing the interaction mechanisms that take place within a granular flow, such as rolling of individual particles or overall turbulence, should be used. This perspective seems far-fetched since the mechanisms to be reproduced are very complex.

## 5 Conclusions

In this study, we analysed how a granular material flows down a slope using both the MPM and DEM in order to test the relevance of two types of numerical methods (discrete and continuous) in terms of kinematics of granular avalanches (propagation distances and amounts of dissipated energies). For this, different container shapes, internal block shapes (DEM), heights of release and friction coefficients were used.

It was found that from the parameters chosen, the basal friction coefficient seems to have the strongest influence on the outcome. This determined the different types of behaviours that can be found during the propagation of a granular material. Overall, it was found that for low basal friction coefficients, the material tends to dissipate energy mostly in the form of friction with the surface and there is very little energy dissipated internally due to normal contact with the surface. In this case, simulations using both methods showed very similar results quantitatively and qualitatively. For medium basal friction coefficients, some shearing within the material started to occur, and while the means of dissipation remained frictional, a different behaviour started to surface, where in the MPM simulations the material underwent some shearing while in the DEM simulations some rolling and sliding of the cubic blocks took place. The means of energy dissipation between the two methods started to diverge, but results in terms of spreading of the deposit and runout distance between the two methods still matched. Lastly, for high basal friction coefficients, the behaviour that started to surface with medium basal friction coefficients was intensified. In this case, correlations between the two methods were only found when the rolling of the blocks was hindered, that is, when brick-shaped blocks were utilised. These correlations happened in terms of runout distance and spread of the deposit. For MPM, an increase of the basal friction angle induces systematically an increase of the basal and internal dissipative energies. For DEM, when using cubes which are prone to rotate on the slope and to slide on the horizontal plane, an increase of the basal friction angle leads to minor changes in total energy dissipated on the slope

and major changes on the horizontal plane consecutively to the increase of basal dissipation. When using elongated elements, sliding mechanisms and basal friction become more influent so that the DEM and MPM results, governed by rather similar mechanisms, are rather equivalent in terms of positions of mass deposit. To reproduce this difference of behaviour in MPM inherent to DEM block shape seems to be a hard challenge to solve.

In general, the study shows that the MPM is capable of modelling the behaviour described by the DEM under certain conditions, specially in terms of runout distance and spread of the deposit. This holds true for cases where the flow happens along a slope, as in the cases presented in this study. For conditions where the topography includes much larger irregularities, such as cliff, the DEM would prevail as the better method to simulate this type of phenomena. In spite of that, the results found in this study are encouraging, given that the constitutive law used to model the behaviour of the soil in MPM was a rather simple law (Mohr-Coulomb). Probably, some more advanced constitutive laws such as the "$\mu(I)$ law" [13] should be able to better reproduce some aspects of the granular flow, as internal dissipation due to collision or rotation of elements. Nevertheless, complex mechanisms like those induced at the base of the flow considering cubes or elongated element on the slope or on the horizontal plane seem complex to integrate.

**Acknowledgements** This work was supported and funded by IMSRN company (headed by Pierre Plotto) and ANRT (French ministry: Ministère de l'Enseignement supérieur, de la Recherche et de l'Innovation).

## References

1. Banton J, Villard P, Jongmans D, Scavia C (2009) Two-dimensional discrete element models of debris avalanches: parameterization and the reproducibility of experimental results. J Geophys Res 114(F4):F04013. https://doi.org/10.1029/2008JF001161
2. Bardenhagen SG, Kober EM (2004) The generalized interpolation material point method. CMES Comput Model Eng Sci 5(6):477–495. https://doi.org/10.3970/cmes.2004.005.477
3. Belytschko T, Lu YY, Gu L (1994) Element-free Galerkin methods. Int J Numer Methods Eng 37(2):229–256. https://doi.org/10.1002/nme.1620370205
4. Bottelin P, Jongmans D, Daudon D, Mathy A, Helmstetter A, Bonilla-Sierra V, Cadet H, Amitrano D, Richefeu V, Lorier L, Baillet L, Villard P, Donz F (2014) Seismic and mechanical studies of the artificially triggered rockfall at the mount neron (french alps, december 2011). Nat Hazards Earth Syst Sci 14(2):3175–3193
5. Brackbill J, Ruppel H (1986) FLIP: a method for adaptively zoned, particle-in-cell calculations of fluid flows in two dimensions. J Comput Phys 65(2):314–343. https://doi.org/10.1016/0021-9991(86)90211-1
6. Brackbill JU, Kothe DB, Ruppel HM (1988) Flip: a low-dissipation, particle-in-cell method for fluid flow. Comput Phys Commun 48(1):25–38. https://doi.org/10.1016/0010-4655(88)90020-3
7. Brannon R, Burghardt JA, Bronowski D, Bauer S (2009) Experimental assessment of unvalidated assumptions in classical plasticity theory, Report No.: SAND2009-0351, Grant Number: AC04-94AL85000, Sandia National Laboratories (Pub.). https://doi.org/10.2172/948711
8. Cleary PW, Prakash M (2004) Discrete-element modelling and smoothed particle hydrodynamics: potential in the environmental sciences. Philos Trans R Soc A Math Phys Eng Sci 362(1822):2003–2030. https://doi.org/10.1098/rsta.2004.1428
9. Cundall P (1971) A computer model for simulating progressive, large scale movement in blocky rock systems. In: Proceedings of the symposium of the international society for rock mechanics, society for rock mechanics (ISRM), Nancy, France, vol 2, pp 129–136
10. Cundall PA, Strack ODL (1979) A discrete numerical model for granular assemblies. Géotechnique 29(1):47–65. https://doi.org/10.1680/geot.1979.29.1.47
11. Gingold RA, Monaghan JJ (1977) Smoothed particle hydrodynamics: theory and application to non-spherical stars. Mon Not R Astron Soc 181(3):375–389. https://doi.org/10.1093/mnras/181.3.375
12. Harlow FH (1957) Hydrodynamic problems involving large fluid distortions. J ACM 4(2):137–142. https://doi.org/10.1145/320868.320871
13. Jop P, Forterre Y, Pouliquen O (2006) A new constitutive law for dense granular flows. Nature 441:1–13
14. Mangeney-Castelnau A (2003) Numerical modeling of avalanches based on Saint Venant equations using a kinetic scheme. J Geophys Res 108(B11):2527. https://doi.org/10.1029/2002JB002024
15. Manzella I, Labiouse V (2009) Flow experiments with gravel and blocks at small scale to investigate parameters and mechanisms involved in rock avalanches. Eng Geol 109(1–2):146–158. https://doi.org/10.1016/j.enggeo.2008.11.006
16. Manzella I, Labiouse V (2013) Empirical and analytical analyses of laboratory granular flows to investigate rock avalanche propagation. Landslides 10(1):23–36. https://doi.org/10.1007/s10346-011-0313-5
17. McDougall S, Hungr O (2004) A model for the analysis of rapid landslide motion across three-dimensional terrain. Can Geotech J 41(6):1084–1097. https://doi.org/10.1139/t04-052
18. Mollon G, Richefeu V, Villard P, Daudon D (2012) Numerical simulation of rock avalanches: influence of a local dissipative contact model on the collective behavior of granular flows. J Geophys Res Earth 117(F2):F02036. https://doi.org/10.1029/2011JF002202
19. Mollon G, Richefeu V, Villard P, Daudon D (2015) Discrete modelling of rock avalanches: sensitivity to block and slope geometries. Granul Matter 17(5):645–666. https://doi.org/10.1007/s10035-015-0586-9
20. Moresi L, Dufour F, Mühlhaus HB (2003) A Lagrangian integration point finite element method for large deformation modeling of viscoelastic geomaterials. J Comput Phys 184:476–497. https://doi.org/10.1016/S0021-9991(02)00031-1
21. Okura Y, Kitahara H, Sammori T, Kawanami A (2000) Effects of rockfall volume on runout distance. Eng Geol 58(2):109–124. https://doi.org/10.1016/S0013-7952(00)00049-1
22. Pirulli M, Bristeau MO, Mangeney A, Scavia C (2007) The effect of the earth pressure coefficients on the runout of granular material. Environ Model Softw 22(10):1437–1454. https://doi.org/10.1016/j.envsoft.2006.06.006
23. Richefeu V, Mollon G, Daudon D, Villard P (2012) Dissipative contacts and realistic block shapes for modeling rock avalanches. Eng Geol 149–150:78–92. https://doi.org/10.1016/j.enggeo.2012.07.021

24. Stoker H (1999) Developments of the arbitrary lagrangian-eulerian method in non-linear solid mechanics applications to forming processes. Universiteit Twente, Enschede
25. Sulsky D, Brackbill JU (1991) A numerical method for suspension flow. J Comput Phys 96(2):339–368. https://doi.org/10.1016/0021-9991(91)90240-L
26. Sulsky D, Chen Z, Schreyer HH (1994) A particle method for history-dependent materials. Comput Methods Appl Mech 118:179–196. https://doi.org/10.1016/0045-7825(94)90112-0
27. Taboada A, Estrada N (2009) Rock-and-soil avalanches: theory and simulation. J Geophys Res Solid Earth 114(3):1–23. https://doi.org/10.1029/2008JF001072
28. Tommasi P, Campedel P, Consorti C, Ribacchi R (2008) A discontinuous approach to the numerical modelling of rock avalanches. Rock Mech Rock Eng 41(1):37–58. https://doi.org/10.1007/s00603-007-0133-z
29. Valentino R, Barla G, Montrasio L (2008) Experimental analysis and micromechanical modelling of dry granular flow and impacts in laboratory flume tests. Rock Mech Rock Eng 41(1):153–177. https://doi.org/10.1007/s00603-006-0126-3
30. Wood DM (1991) Soil behaviour and critical state soil mechanics. Cambridge University Press, Cambridge. https://doi.org/10.1017/CBO9781139878272
31. Zhou GG, Sun QC (2013) Three-dimensional numerical study on flow regimes of dry granular flows by DEM. Powder Technol 239:115–127. https://doi.org/10.1016/j.powtec.2013.01.057
32. Zienkiewicz OC, Taylor RLRL (2005) The finite element method for solid and structural mechanics. Elsevier Butterworth-Heinemann, Oxford

**Publisher's Note** Springer Nature remains neutral with regard to jurisdictional claims in published maps and institutional affiliations.